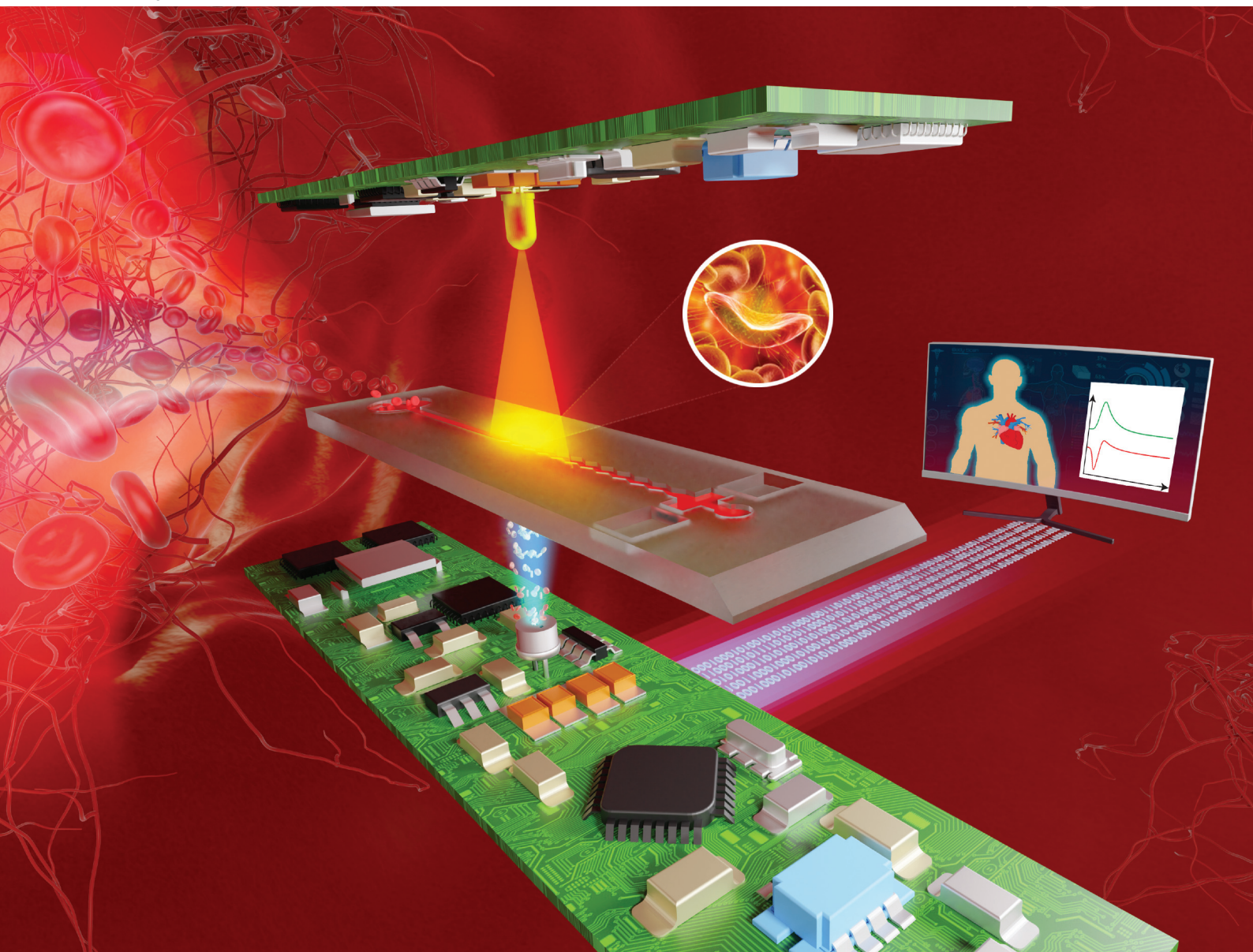


Analyst

rsc.li/analyst



ISSN 0003-2654

PAPER

Caglar Elbuken *et al.*
In vitro analysis of multiple blood flow determinants using
red blood cell dynamics under oscillatory flow



Cite this: *Analyst*, 2020, **145**, 5996

In vitro analysis of multiple blood flow determinants using red blood cell dynamics under oscillatory flow†

Ziya Isiksacan,^a Murat Serhatlioglu^a and Caglar Elbuken *^{a,b}

The flow behavior of blood is determined mainly by red blood cell (RBC) deformation and aggregation as well as blood viscoelasticity. These intricately interdependent parameters should be monitored by health-care providers to understand all aspects of circulatory flow dynamics under numerous cases including cardiovascular and infectious diseases. Current medical instruments and microfluidic systems lack the ability to quantify these parameters all at once and in physiologically relevant flow conditions. This work presents a handheld platform and a measurement method for quantitative analysis of multiple of these parameters from 50 μl undiluted blood inside a miniaturized channel. The assay is based on an optical transmission analysis of collective RBC deformation and aggregation under near-infrared illumination during a 1 s damped oscillatory flow and at stasis, respectively. Measurements with blood of different hemo-rheological properties demonstrate that the presented approach holds a potential for initiating simultaneous and routine on-chip blood flow analysis even in resource-poor settings.

Received 27th March 2020,

Accepted 11th June 2020

DOI: 10.1039/d0an00604a

rsc.li/analyst

Introduction

Blood flow-related disorders are responsible for a quarter of all deaths across the world.¹ Interdependent hemo-rheological² parameters, comprising mainly deformation and aggregation of red blood cells (RBC) and blood viscoelasticity, are the determinants of blood flow in vascular networks.^{3,4} Acquired or hereditary diseases affecting one parameter cause alterations in others, such as hyperviscosity syndrome as a result of anemia originated in decrease in RBC deformation.⁵ Another example is that storage-induced lesions like RBC stiffness cause alterations in multiple parameters, paving the way for severe complications following blood transfusion.^{6,7} Presently, these parameters are rarely, if not at all, measured in clinics due to the drawbacks of using several benchtop instruments, requiring highly skilled and diversified workforce, lab space, high sample volume, operation time, and a large budget.⁸ An all-at-once measurement approach also remains elusive thus far in the microfluidics community. There are only a few studies analyzing two parameters at a time based on image

processing.^{9,10} This manuscript addresses a novel point-of-care solution for the rapid analysis of multiple hemo-rheological parameters (RBC deformation, RBC aggregation, and blood/plasma viscoelasticity) from an undiluted blood sample without requiring cleanroom fabricated chips or microscopy setups.

Human RBCs are anucleated discoid cells of 6–8 μm diameter with a 10 nm viscoelastic membrane. They constitute around 2/3 of all body cells and 1/2 of blood volume, amounting to an RBC count of 20–30 trillion in the circulatory system of a healthy adult.^{11,12} Deformability of RBCs is essential for oxygen delivery through capillary networks. Numerous pathological changes in the RBC membrane, skeleton, and interior cause RBC stiffness, which potentially results in capillary blockage (malaria, diabetes, and sickle cell disease) and insufficient oxygen supply to tissues.^{13,14} To date, most RBC characterization methods focus on a single aspect of these cells at a low throughput, obscuring an understanding of the overall flow characteristics. Cell deformation is quantified by micropipette aspiration,¹⁵ atomic force microscopy,¹⁶ flow cytometry,¹⁷ and optical tweezers.¹⁸ There is also an extensive literature on microfluidic techniques for RBC deformability. The operating principles of platforms include cell blockage,¹⁹ transit (velocity, margination, and sorting),²⁰ and impedance analysis²¹ for the characterization of malaria-infected or hardened RBCs. These platforms have not yet found a ground in clinics possibly due to costly chip fabrication, requirement for sample

^aUNAM – National Nanotechnology Research Center and Institute of Materials Science and Nanotechnology, Bilkent University, 06800 Ankara, Turkey.
E-mail: elbuken@unam.bilkent.edu.tr

^bFaculty of Biochemistry and Molecular Medicine, Faculty of Medicine, University of Oulu, 90014 Oulu, Finland

†Electronic supplementary information (ESI) available. See DOI: 10.1039/d0an00604a

processing (dilution), and the need for off-chip components such as pumps and microscopes.

RBC aggregation is the formation of face-to-face RBC clumps at low shear rates and stasis.²² This mechanism is reversible and affected by cellular properties (surface charge and deformability), medium properties (viscosity and protein level), and flow properties (shear rate). The shear rate of blood flow in healthy circulation is above 10 s^{-1} where RBCs do not form aggregates. However, clinical conditions slowing down blood flow and affecting medium/cell properties (like elevated fibrinogen concentration) cause aggregation that may lead to hyperviscosity or vascular occlusion. Such conditions include various viral infections, inflammations, multiple myeloma, and diabetes.⁵ Microfluidic platforms based on electrical conductivity,²³ optical analysis,^{24,25} or microscopy imaging²⁶ can currently measure RBC aggregation.

Blood consists of plasma and cells (mostly deformable RBCs), and as such, is a shear-thinning viscoelastic fluid.²⁷ Clinical range blood viscosity is associated with diseases such as myocardial infarction and hypertension.²⁸ Rheometers, viscometers, and recently various microfluidic techniques like co-flow analysis, advancing meniscus monitoring, or impedimetric detection can be used for blood/plasma viscosity measurement.³ Blood elasticity measurement is also not a routine clinical practice. The elastic behavior of blood was thought to originate solely from RBCs.²⁹ A recent study using a capillary breakup rheometer has demonstrated the viscoelastic nature of plasma.³⁰ Nevertheless, the relationship between blood/plasma viscoelasticity and flow disorders (cardiovascular diseases) has not been entirely conceived and should be further elucidated. More specifically, a complete analysis of RBC deformation, RBC aggregation, and blood/plasma viscoelasticity could markedly increase the safety of blood transfusion.³¹ The RBCs of donated blood undergo alterations during the conventional 42 days of cold storage (*e.g.*, decreasing deformability, and increasing viscosity).³² Hence, the use of untested non-fresh blood causes potential complications including organ failure and mortality.³³

Microfluidic technologies possess a significant potential for the assessment of hemo-rheological parameters and help diagnose unhealthy blood flow. Herein, we report a portable device for the analysis of multiple parameters from $50 \mu\text{l}$ blood in 3 min. The assay principle is based on the optical transmission analysis of RBC deformation and aggregation in an undiluted blood sample. The test starts off by sample introduction to a rigid, straight channel of a disposable polycarbonate

cartridge. This is followed by a 1 s reciprocating sample motion with gradually decreasing stroke distances, initiated by an integrated displacement pump. The sample is illuminated in the near-infrared band with a wavelength of 830 nm where hemoglobin absorption is minimum. Optical transmission through the sample is recorded during flow (14 s) and then at stasis (126 s) to optically quantify RBC deformation and aggregation, respectively. Medium viscosity, medium elasticity, RBC stiffness, and RBC aggregability are varied one at a time to obtain blood samples with different hemo-rheological properties, and the measured optical signals are shown to be responsive to corresponding alterations. The analysis is carried out in a channel environment that mimics vascular flow: confined, directional, pulsatile movement of blood at shear rates and RBC volume fractions comparable to physiological levels. Finally, the portability of the analyzer (200 g), use of small sample volume ($50 \mu\text{l}$), short assay time (3 min), and low-cost disposable cartridges (US\$ 0.02) are noteworthy for point-of-care adaptation of the presented novel technique.

Experimental section

Blood collection

Ethical approval was obtained from the Ethics Committee of Bilkent University (Ankara, Turkey), and all experiments were performed in compliance with the institutional guidelines. Informed consent was obtained from the human participant.

10 ml of fresh whole blood with 47% RBC volume fraction was acquired from a healthy male volunteer into a sodium citrate containing vacuum tube. The blood was centrifuged and washed three times with $1\times$ phosphate-buffered saline (PBS), keeping the RBC volume fraction constant. Following blood withdrawal, the sample was kept at $25 \text{ }^\circ\text{C}$ and used within 6 h.

Suspending medium preparation

(See Table 1) Blood plasma has a relaxation time of 0.1 ms. Hence, a plasma replacement medium with a relaxation time of 0.1 ms was prepared by dissolving 0.0085% w/v polyethylene oxide polymer (PEO; $M_w = 600 \text{ kDa}$, Sigma-Aldrich) in $1\times$ PBS (ESI Note 1†). Glycerol (Sigma-Aldrich) was mixed with the plasma replacement solution at three concentrations (5%, 10%, 20% v/v) to obtain three media for viscosity analysis. PEO was dissolved in $1\times$ PBS at three concentrations (0.05%, 0.1%,

Table 1 Summary of the rheological properties (η : viscosity and λ : relaxation time) of the suspending media

Suspending Medium	Solvent	PEO in solvent (w/v)	η [mPa s]	λ [ms]
Medium 1	5% Glycerol & 95% PBS	0.0085%	0.98	0.099
Medium 2	10% Glycerol & 90% PBS	0.0085%	1.14	0.099
Medium 3	20% Glycerol & 80% PBS	0.0085%	1.53	0.099
Medium 4	100% PBS	0.05%	1.40	0.312
Medium 5	100% PBS	0.1%	1.57	0.490
Medium 6	100% PBS	0.2%	2.41	0.768

0.2% w/v) to obtain three additional media for elasticity analysis.

Blood sample preparation

(See Table S2† for summary) Healthy RBCs have a shape recovery time of 0.15–0.30 s following deformation.^{13,34} Six different blood samples (H-samples 1 to 6; H for healthy) were prepared by suspending healthy RBCs (47% v/v) in media 1 to 6, respectively. To obtain RBCs with stiffened cell membranes, the healthy RBCs suspended in 1× PBS (47% v/v) were treated with 0.025% v/v glutaraldehyde (GA) solution, which was prepared in 1× PBS from a 25% w/v stock GA (Sigma-Aldrich). 0.025% v/v GA fixation increases RBC rigidity around 4 times.³⁵ Then, six additional blood samples (S-samples 1 to 6; S for stiffened) were prepared by suspending stiffened RBCs (47% v/v) in media 1 to 6, respectively. 70 kDa Dextran (Sigma-Aldrich) was added to three blood samples (healthy RBCs suspended in 1× PBS, 47% v/v) at different concentrations to change RBC aggregability (A-samples 1 to 3; A for aggregated). Dextran concentrations for three suspending media were 10 mg ml⁻¹, 20 mg ml⁻¹, and 40 mg ml⁻¹, respectively.

Rheological measurements

A rotational rheometer (MCR 301, Anton Paar) was used for the viscosity (η) measurement of the six suspending media (Fig. S1†). The measuring unit has a 50 mm diameter cone plate geometry (CP50-1).

Constant shear rate mode was chosen, and the temperature was set to 25 °C. A 760 μ l sample was used for each measurement. The shear rate was swept from 10 to 1000 s⁻¹. The relaxation times (λ) of the suspending media were calculated using the Zimm estimation (ESI Note 1†). All rheological values are given in Table 1.

Pump characterization

The pressure generated by the pump was characterized using a pressure sensor (40PC015 G, Honeywell). A silicone tube was connected to the pump, and the pressure was recorded and

sampled using a data acquisition card (DAQPad-6015, National Instruments).

Image analysis

A 1 s video recording of the blood sample inside a channel was taken using an inverted optical microscope (Zeiss Axio Vert) equipped with a high-speed camera (Phantom Miro 2) at 2.5× magnification. The recording rate was 2800 frame per second. Images were obtained from the video using the camera software.

Cartridge fabrication

The cartridge had a single straight fluidic channel (depth (d), width (w) = 1 mm; length (l) = 50 mm) with one inlet and outlet. It was designed using CAD software (AutoCAD 2007). For initial prototyping and channel optimization, the cartridges were fabricated out of poly(methyl methacrylate) (PMMA) using CO₂ laser ablation.³⁶ Then, a metal mold was fabricated using CNC machining, and the transparent polycarbonate rigid cartridges were mass-fabricated by injection molding following industrial standards.

Measurement platform

Fig. 1 shows the schematic illustration and photograph of the portable device that consists of three main elements: integrated pump, optical detection unit (light-emitting diode and phototransistor), and microprocessor (also see Fig. S2† for workflow). Following a 50 μ l sample introduction into the single channel of the cartridge and cartridge insertion into a 3D printed cartridge holder at room temperature, an airtight fluidic connection was made between the channel outlet and the pump. With the start of the test, the pump mechanically moves an actuator pin forward and backward with 0.5 s⁻¹ frequency for a duration of 14 s (ESI Movie 1†). Each forward pin movement generates 12.5 mbar pressure driving the sample forward inside the channel with 5 mm stroke distance and initiates a 1 s damped oscillatory flow (Fig. 2a). Meanwhile, an 830 nm wavelength near-infrared light-emitting diode (LED;

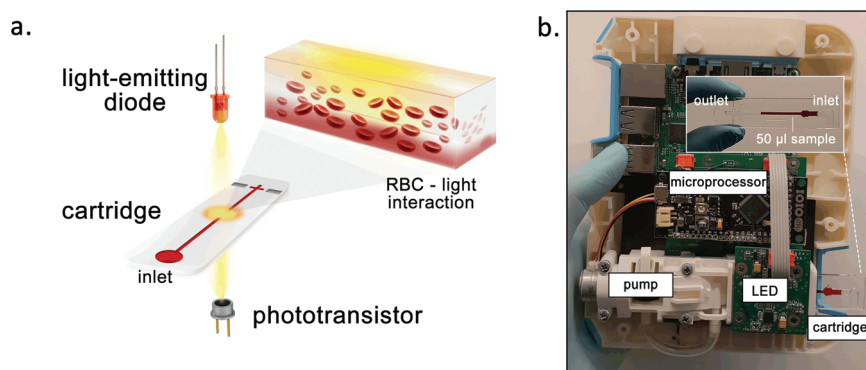


Fig. 1 Schematics and photograph of the device. (a) Schematic representation. Collective RBC movements are optically investigated under near-infrared illumination. Analysis takes place in a channel. (b) Handheld device developed for the implementation of the optical method. Inset. Transparent disposable cartridge has a straight channel (depth = width = 1 mm, length = 50 mm) filled with a 50 μ l blood sample.

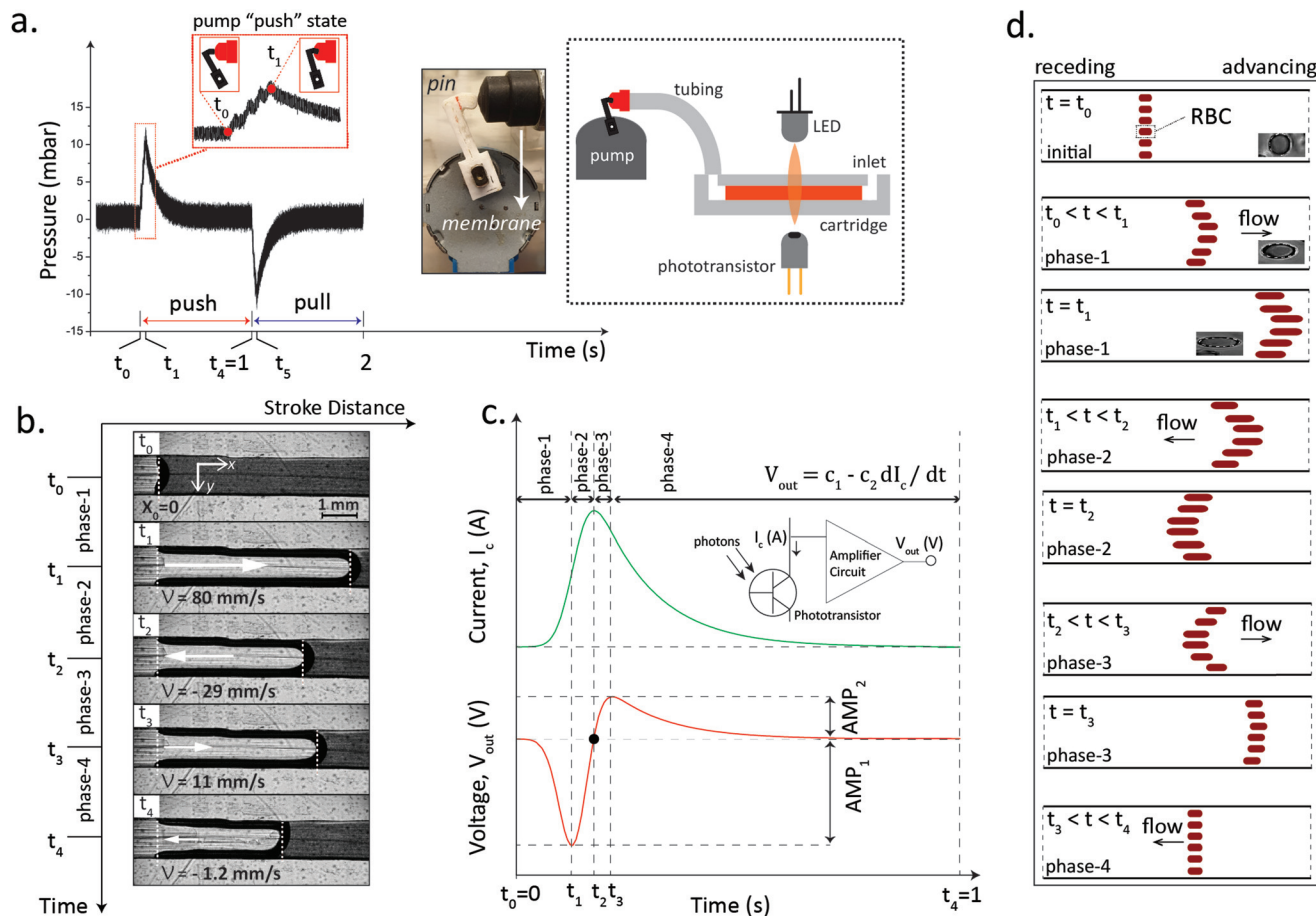


Fig. 2 (a) Pump characterization. Pressure generated by the pump during one cycle comprising a 1 s push state and a 1 s pull state. (b) Side-view images of a 1 s oscillatory flow from a high-speed camera recording. The observation window is near the receding edge (see Fig. S3†) for easier comparison for different phases. Stroke distances and velocities are displayed on images. (c) Output signals measured by the device during 1 s oscillatory flow. Current signal measured directly from the phototransistor output and voltage signal measured as the output of the analog amplifier circuit fed by the current signal. Both signals are divided into four distinct phases. (d) Schematic cross-sectional side-view model of collective RBC movements during a 1 s oscillatory flow. Microscopy images demonstrate the progression of a single RBC deformation during shear flow.

Vishay) illuminates the blood sample, and an NPN phototransistor (Vishay) collects the light transmitting through the sample in the form of an electrical current. The near-infrared band of the electromagnetic spectrum at which the LED works minimizes the photon absorption by hemoglobin (proteins confined in RBCs) and therefore enhances the transmission through the blood sample. RBC deformation during a flow reduces RBCs' surface area to volume ratio giving photons more space to pass through the sample.^{37,38} Transmission intensity, that is, measured electrical current, is higher for RBCs deformed at shear flow compared to the disaggregated suspended RBCs at stasis. Likewise, individually suspended RBCs result in lower transmission intensity at stasis, and as they aggregate, the intensity level increases.^{25,39} Hence, we quantified (I) RBC deformation during flow and (II) RBC aggregation at stasis by measuring the transmission intensity (electrical current) using the phototransistor. The current output (I_c [mA]) passes through an analog circuit consisting of a transimpedance amplifier, a lowpass filter, and

an amplifying differentiator to obtain a voltage output (V_{out} [mV]) such that

$$V_{out} = c_1 - c_2 dI_c / dt \quad (1)$$

where c_1 and c_2 are constants. While the current output quantifies RBC deformation, the voltage output gives an understanding of the rate of RBC deformation at specific time intervals of optical measurement. The resulting analog voltage signal is digitized using the microprocessor and analyzed using MATLAB (R2018, MathWorks). Assay parameters such as LED intensity, test duration, and pressure can be tuned with a microprocessor (IOIO OTG, SparkFun).

Results and discussion

Optical analysis of RBC movements in a fluidic channel

During the test, the displacement pump moves the actuator pin forward and backward for 14 s. Fig. 2a depicts one cycle of

the pressure generated by the pump. The pump action consists of a 1 s push state and a 1 s pull state (ESI Movie 1†). At the start of the cycle (t_0), the pin is in contact with an elastic membrane that makes an airtight connection to the channel outlet. In the push state, the pin pushes the membrane inward for 60 ms compressing the air within the system to generate an increasing pressure with a maximum value of 12.5 mbar at t_1 . Following t_1 , the pressure decreases and finally attenuates to zero at the end of 1 s (t_4). For the push state (t_0 to t_4), the initial pin movement (t_0 to t_1 ; $\Delta t_1 = 60$ ms) initiates a 1 s oscillatory flow of the sample within the channel (ESI Movie 2†). We are interested in the push state for the optical measurements. In the pull state, the pin withdraws, letting the membrane retract to its undeformed position.

To understand the flow dynamics, a microscope is used to obtain a side-view video recording of the blood sample inside the channel (not necessary for routine use of the system). Fig. 2b shows the side-view images of a 1 s oscillatory flow during a push state (ESI Movie 2†) at an observation window near the sample receding edge (also see Fig. S3†). The sample is stationary at t_0 . Then, the pin pushes the adaptor for 60 ms, driving the sample forward, reaching a stroke distance of 5 mm at t_1 ($\Delta t_1 = 60$ ms). During this bulk motion, a small layer of fluid remains attached to the channel walls due to adhesion between the walls and fluid. Hence, although the pin stops at t_1 , the bulk fluid moves backward for 1 mm until t_2 ($\Delta t_2 = 42$ ms) because of the cohesive forces between the fluids on the wetted walls and bulk. Again, the wetting on the advancing edge (not shown) causes a small forward flow until t_3 ($\Delta t_3 = 36$ ms). Finally, the fluid moves backward very slowly (mean velocity: 1.2 mm s^{-1}) for 860 ms until t_4 . There are apparently four phases of sample flow. The sample has a different velocity in each phase. This results in different wall shear rates (phase-1: 480 s^{-1} ; phase-2: 174 s^{-1} ; phase-3: 66 s^{-1} ; phase-4: 7.2 s^{-1}) that we approximately calculated using eqn (2), which is used for a rectangular channel profile ($d/w \leq 1$), where $\dot{\gamma}$ and Q are the wall shear rate and flow rate, respectively.⁴⁰

$$\dot{\gamma} = 6Q/wd^2 \quad (2)$$

Microscopy images of the oscillatory flow in Fig. 2b reveal the differences in flow rates, and hence wall shear rates, for each phase. The shear rate determines the shear stress experienced by RBCs that, as a result, deform longitudinally to accommodate the stress. During the experiments, we measure physical changes in collective RBC deformation in the 1 s push states by illuminating the blood sample and collecting the transmitted light using the phototransistor. Fig. 2c illustrates an example of the current signal measured directly from the phototransistor during a 1 s oscillatory flow as well as the corresponding voltage signal obtained after analog processing (amplification and differentiation) of the current signal. As in Fig. 2b, the current signal consists of four distinct phases. The signal is concave-up with an increasing positive slope (phase-1), followed by a continuation of the rise with a decreasing slope (phase-2). After t_2 where the current is at maximum, the

signal is concave-down with a decreasing negative slope (phase-3), and it goes back to the initial level (phase-4). The distinction between current levels in these phases, *viz.* RBC deformation in these phases, can be more clearly understood in the voltage signals that represent the rate of deformation. The voltage signal forms two peaks ($AMP_{1,2}$) at the end of phase-1 and phase-3, respectively. It has a zero crossing when the current is at maximum (t_2), and it settles down to the initial voltage level at the end of phase-4 (t_4).

The dense population of RBCs in the channel, because of the clinically relevant RBC volume fraction and the channel depth, hinders the observation of individual RBCs under a microscope. Based on the microscopy observation of the bulk sample shown in Fig. 2b and the corresponding optical transmission analyses in Fig. 2c, a 1 s four-phase oscillatory flow is schematically summarized in Fig. 2d. ($t = t_0$) RBCs are arbitrarily suspended in the medium. Phase 1: ($t_0 < t < t_1$) The sample moves forward. The RBCs align with the Poiseuille flow and deform longitudinally in response to increasing shear stress. The current level increases because the RBCs are deformed, allowing more light transmission. ($t = t_1$) Pump pressure is at a maximum. The RBCs have the largest rate of deformation. Hence, the voltage output forms a peak, AMP_1 . Phase 2: ($t_1 < t < t_2$) The wetting effect on the receding edge moves the sample backward. The RBCs align with the flow and deform longitudinally. The current level increases due to RBC deformation. The shear stress generated by the wetting effect (0.15 Pa) is smaller than the stress generated by the pump (0.43 Pa). Therefore, deformation is smaller at $t_1 < t < t_2$ than at $t_0 < t < t_1$. ($t = t_2$) The RBCs have the highest backward deformation. The voltage output reaches the zero crossing. Phase 3: ($t_2 < t < t_3$) The wetting effect on the advancing edge moves the sample forward. The RBCs start regaining their original shape due to fading shear stress. The current level decreases when the deformation decreases and the second largest rate of deformation is attained at t_3 where the voltage output forms another peak, AMP_2 . Phase 4: ($t_3 < t < t_4$) RBCs move backward very slowly until their complete stop and shape recovery at $t = t_4$. The current level gradually falls to the initial level.

Change in medium properties

Viscoelastic plasma is a suspending medium for RBCs, and its rheology is a key determinant of overall blood flow. Specifically, medium viscoelasticity determines the generation of viscous and elastic stresses applied on RBCs, thereby determining RBC deformation during flow. Viscous stresses facilitate RBC deformation, whereas elastic stresses suppress it. Hence, an increase in medium viscosity or a decrease in medium elasticity enhances RBC deformation^{41,42} and thus optical transmission. We prepared suspending media with different viscoelastic properties (Table 1) to confirm this. Firstly, three media were prepared using varying concentrations of glycerol during the plasma replacement (media 1, 2, and 3). Using these media, three blood samples (H-samples 1, 2, and 3) were prepared from healthy, deformable RBCs (47% v/v).

Fig. 3a shows the average optical signal corresponding to seven repetitive 1 s oscillatory flows (Fig. S4a†) for these samples. Fig. 3b compares the optical signal parameters (AMP_1 and AMP_2) with the glycerol concentration. $AMP_{1,2}$ increase with the increasing medium viscosity, while t_2 (Fig. S5a†) remains the same. As demonstrated in Fig. 2b, in phase-1, the pump generates an increasing pressure to drive the sample forward. In the meantime, shear stress (τ) applied on the RBCs deforms the cells. Given that the shear rate ($\dot{\gamma}$) is a function of flow rate (Q) and is the same for all the samples during phase-1 (eqn (2)), an increase in medium viscosity (η) increases the shear stress as follows:

$$\tau = \eta\dot{\gamma} = \eta \cdot 6Q/wd^2 \quad (3)$$

The increasing shear stress in phase-1 accordingly deforms the RBCs more, which eventually increases light transmission and AMP_1 . Therefore, given the same elasticity, the more viscous the medium, the higher the rate of deformation and AMP_1 value.

Pressure is the dominant factor in determining the flow rate in phase-1 and phase-2, given the short time scales of these phases ($\Delta t_1 = 60$ ms, $\Delta t_2 = 40$ ms). Hence, t_2 only negligibly increases with the increasing medium viscosity.

The RBCs are in a deformed state at t_2 . During phase-3, they lose their deformation due to fading shear stress (Fig. 2b), and they partially recover their undeformed shape at t_3 . The more viscous the medium, the higher the stress change (eqn (3)). This consequently results in a higher rate of deformation

leading to a higher intensity change. Hence, a higher AMP_2 is measured in higher viscosity media.

Secondly, three media are prepared using varying concentrations of PEO in PBS (media 4, 5, and 6). Fig. 3c shows the average optical signal for seven repetitive 1 s oscillatory flows (Fig. S4b†) for the samples again with healthy RBCs (H-samples 4, 5, and 6). Fig. 3d compares the characteristic signal maxima and minima with the polymer concentration. AMP_1 decreases with the increasing medium elasticity, while AMP_2 increases. t_2 also decreases with the increasing medium elasticity (Fig. S5b†). The relative importance of elastic and viscous forces of a viscoelastic medium can be represented by the Weissenberg number (Wi) as⁴³

$$Wi = \lambda\dot{\gamma} \quad (4)$$

There are non-linear elastic forces in a viscoelastic fluid expressed in terms of normal stress differences, predominantly the first normal stress (N_1) that increases with the polymer concentration:⁴⁴

$$N_1 = 2\lambda\eta\dot{\gamma}^2 \quad (5)$$

N_1 induced in the flow is at the normal direction to the RBC membrane,^{45,46} and the existence of N_1 suppresses RBC deformation during phase-1. Therefore, AMP_1 decreases with the increasing polymer concentration. t_2 is different for each sample. The polymers are stretched by the stress generated in phase-1, and they store elastic stress, the magnitude of which is proportional to the polymer concentration. They discharge this energy and relax in phase-2 (viscoelastic recovery). More

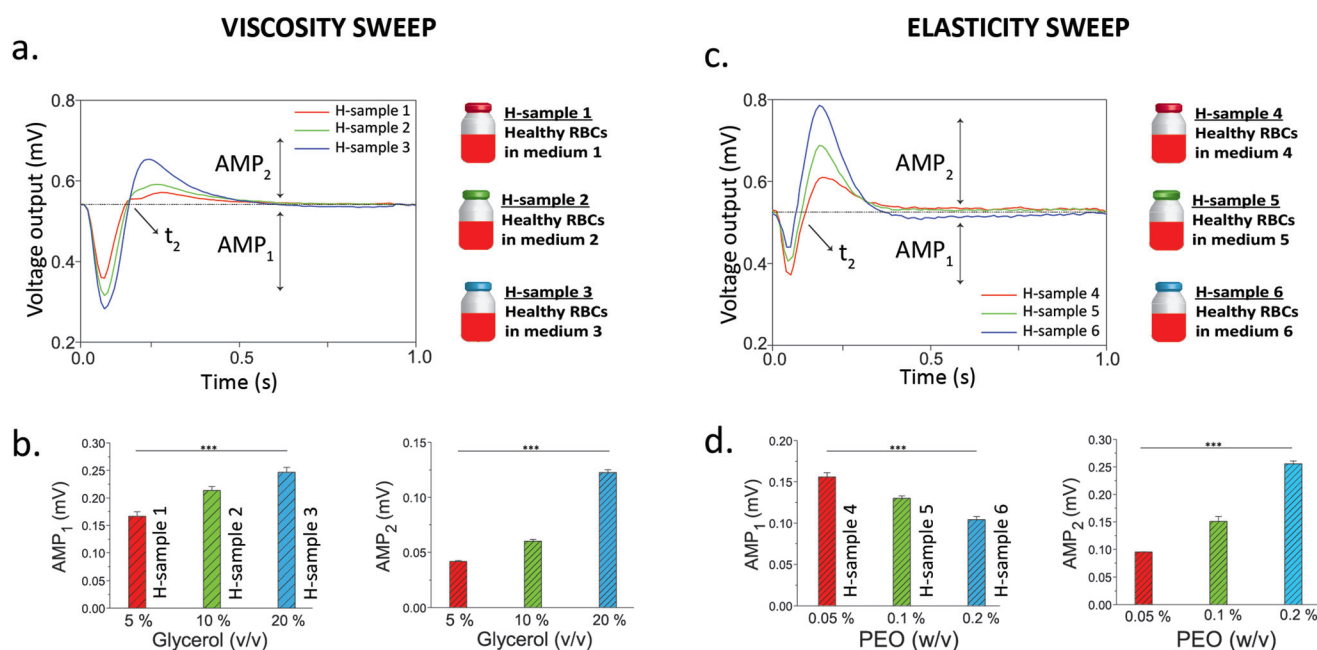


Fig. 3 Effect of suspending medium viscoelasticity on optical transmission signals. Each plot is the average of seven optical signals, obtained from repetitive seven 1 s oscillatory flows, for the following samples: healthy RBCs suspended in (a) media with different glycerol concentrations and (c) media with different PEO concentrations. Comparison of the optical signal parameters (AMP_1 , AMP_2) with (b) the glycerol concentration and (d) the PEO concentration. One-way ANOVA test was used for comparison. The significance is displayed on graphs where *** indicates $p < 0.001$.

elastic samples recover their initial state faster, explained by the creep-recovery response of the Kelvin model as:

$$\varepsilon(t) = Ce^{-(E/\eta)t} \quad (6)$$

where ε , E , η , and C are the strain, sample elasticity, sample viscosity, and initial-state constant, respectively (ESI Note 2†).⁴⁷ Therefore, t_2 is the lowest at the highest polymer concentration, namely the highest E .

The effective relaxation times for all the media are less than 1 ms (Table 1), so the polymers are already relaxed prior to phase-3. Therefore, the media act only in a viscous manner (Newtonian) in phase-3. As in the previous discussion for AMP₂ in Fig. 3b, AMP₂ increases with the increasing medium viscosity.

Having demonstrated the relationship between the optical parameters and the medium viscosity (Fig. 3b) or medium elasticity (Fig. 3d), governing equations relating individual optical parameters to overall medium viscoelasticity can be derived using the viscosity (η_{medium}) and relaxation time (λ_{medium}) values presented in Table 1. Fig. 4a compares $k_1 = [\eta_{\text{medium}}/\lambda_{\text{medium}}]$ to optically measured AMP₁, and Fig. 4b compares $k_2 = [\eta_{\text{medium}}]$ to AMP₂ (recalling that all media act only in a viscous manner in phase-3). Using the regression analysis, two linear equations are obtained as:

$$k_1 = [\eta_{\text{medium}}/\lambda_{\text{medium}}] = a[\text{AMP}_1] + b \quad (7)$$

$$k_2 = [\eta_{\text{medium}}] = c[\text{AMP}_2] + d \quad (8)$$

where a , b , c , and d are constants with the values of 93.1, -7.8 , 6.3, and 0.7, multiplied by 10^{-3} , respectively. This analysis demonstrates that using these equations and the parameters obtained from an optical measurement, medium properties can be calculated as an alternative to the conventional rotational rheometer. In addition, since AMP₁ and AMP₂ are measures of RBC deformation, if the medium properties are already known, these parameters can be employed to obtain the deformation during flow.

Change in RBC membrane stiffness

Healthy RBCs are deformable due to the viscoelastic membranes that enclose the cellular interior. Numerous clinical conditions such as malaria can decrease RBC deformability. We prepared six blood samples (S-samples 1-to-6) by suspending glutaraldehyde-fixed stiffened RBCs inside the six suspending media. Fig. 5 shows the optical measurements for these samples. The trends seen for the H-samples in Fig. 3b&d are also observed for the S-samples in Fig. 5b&d for the same reasons. Briefly, given the same elasticity, AMP_{1,2} increase with the increasing medium viscosity (Fig. 5b) while t_2 remains the same (Fig. S5c†). In addition, AMP_{1,2} decrease with the increasing medium elasticity (Fig. 5d) while t_2 increases (Fig. S5d†). We also observe that due to the compromised deformability of the stiffened RBCs, AMP₁ and AMP₂ are lower for the S-samples compared to those values in the H-samples (Fig. S6†).

RBC aggregation analysis at stasis

RBC aggregation is the main factor determining blood flow at low shear rates. This microfluidic device can also quantify the RBC aggregation of blood. RBCs form aggregates at stasis in a suspending medium containing inducer molecules like dextran, which is a highly water-soluble polysaccharide. The aggregation can be enhanced with increasing dextran concentration, depending on the molecular weight and concentration interval.

Four media were prepared using varying dextran concentrations (0, 10, 20, and 40 mg ml⁻¹) in PBS in which RBC aggregation and solution viscosity⁴⁸ increase linearly with the dextran concentration whereas solution elasticity is negligibly affected.^{49,50} Then, RBCs (47% v/v) were suspended in these media. Fig. 6 shows the corresponding optical transmission measurements, V_{out} . Initially, the pump operates for 14 s, moving the sample back and forth. The generated pressure creates a disaggregating shear rate (phase-1: 480 s⁻¹), which leads to complete disaggregation of the RBCs. At the time the flow ceases, individual RBCs are dis-

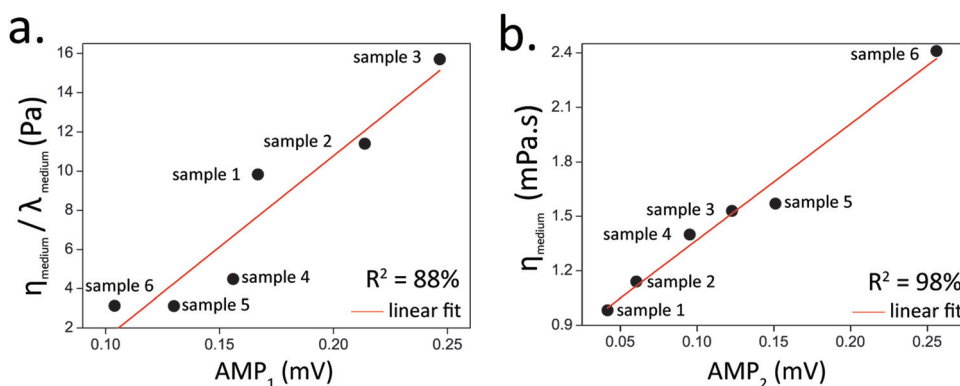


Fig. 4 Comparing optical signal amplitudes to medium properties for the six blood samples with healthy RBCs. (a) The scatter plot and the linear fit comparing AMP₁ to $k_1 = [\eta_{\text{medium}}/\lambda_{\text{medium}}]$. The correlation is 88% using linear regression. (b) The scatter plot and the linear fit comparing AMP₁ to $k_2 = [\eta_{\text{medium}}]$. The correlation is 98% using linear regression.

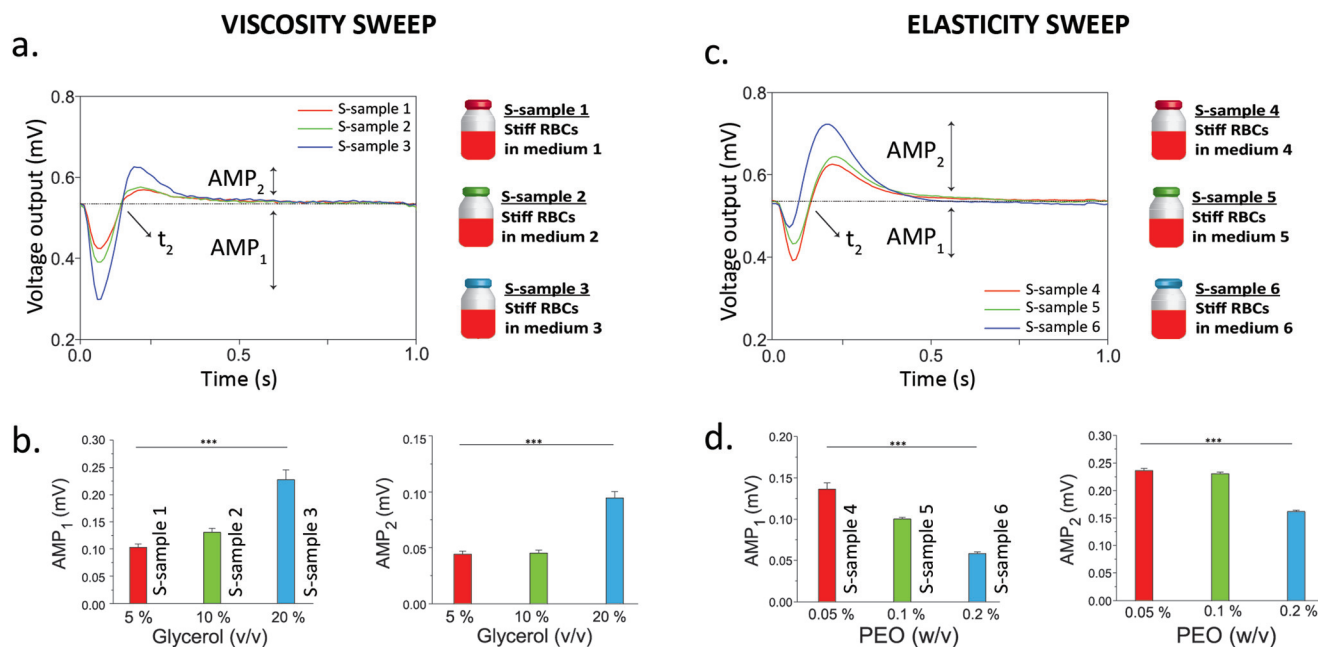


Fig. 5 Effect of suspending medium viscoelasticity on optical transmission signals. Each plot is the average of seven optical signals, obtained from repetitive seven 1 s oscillatory flows, for the following samples: stiffened RBCs suspended in (a) media with different glycerol concentrations and (c) media with different PEO concentrations. Comparison of the optical signal parameters (AMP1, AMP2) with (b) the glycerol concentration and (d) the PEO concentration. One-way ANOVA test was used for comparison. The significance is displayed on graphs where *** indicates $p < 0.001$.

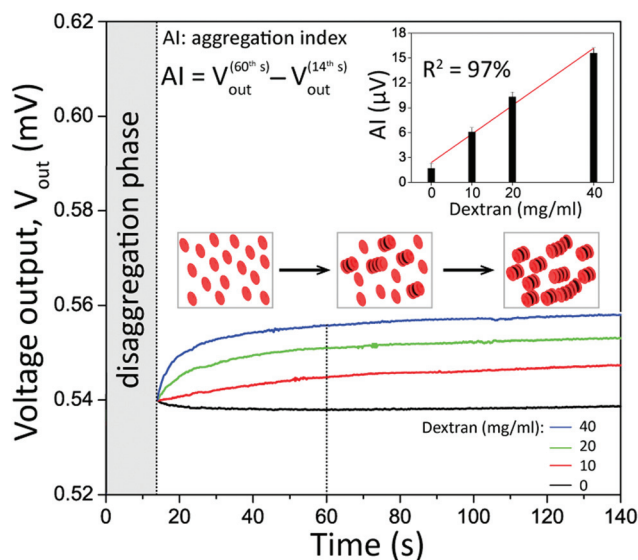


Fig. 6 Optical analysis of RBC aggregation. Four blood samples with different dextran concentrations are prepared. Initial 14 s is for RBC disaggregation. The aggregation process lasts for 140 s. Relative transmission level at the 60th s is taken as the aggregation index (AI). The inset compares AI to dextran concentration. The correlation is 97% using linear regression.

aggregated and dispersed within the channel, resulting in maximum scattering and minimum light transmission. Following the complete disaggregation, the RBCs start to aggregate in the absence of a shear rate until their complete

aggregation at the end of 140th s. The maximum final transmission levels are obtained at the completion of the aggregation phase. The relative transmission level at the 60th s is taken as a measure of RBC aggregation,²² namely the aggregation index (AI) where $AI = [V_{out}^{60th} - V_{out}^{14th}]$. Fig. 6 inset compares AIs for different samples. The correlation between AI and dextran concentration is calculated as 97% using linear regression, confirming the enhancement of aggregation with dextran addition and the ability of our device to quantify it.

Although this manuscript reports the first proof-of-concept study of measuring multiple blood flow determinants using an optical measurement principle on an entirely portable device, it has several limitations that should be addressed in upcoming studies. Firstly, we herein focused on altering one property of the blood sample at a time and observed the resulting changes in the optical signals. For future studies, more than one blood property needs to be swept simultaneously to investigate whether multiple hemorheological parameters can be extracted from the signals. After multiple parameters are quantified from a single measurement, the next step is performing blind tests using clinical samples. Success in clinical trials depends substantially on the availability of conventional equipment (flow cytometer, rheometer, and aggregometer) for benchmarking as well as correlating the blood flow abnormalities to disease states. In addition, a built-in temperature controller unit is needed to keep blood samples at body temperature throughout the test.

Conclusion

We have presented a portable lab-on-a-chip device and a novel measurement method for the determination of multiple hemo-rheological parameters, one at a time, in disposable cartridges from 50 μ l undiluted blood. The operation principle is based on a 3 min optical transmission analysis of collective RBC movements (deformation and aggregation) in a straight single channel under infrared illumination. A unique four-phase damped oscillatory flow mechanism was generated jointly by a displacement pump and wetting effect. The analyses were performed in a miniaturized channel environment that mimicked vascular flow. Optical transmission through the blood sample was recorded during the flow and at stasis to quantify RBC deformation and aggregation, respectively. Blood samples with different medium viscoelasticity and RBC stiffness were employed to experimentally demonstrate that (I) viscous stresses facilitate RBC deformation and (II) elastic stresses suppress it. This presented technique is promising to remove the financial and practical drawbacks associated with the state-of-the-art hemo-rheological analysis methods. Such a sample-in result-out microfluidic approach can eventually make hemo-rheological monitoring accessible in clinics and research labs.

Author contributions

Z. I and C. E conceived and designed the experiments. Z. I and M. S. performed the experiments. All authors discussed the results. Z. I. prepared the figures. Z. I. and C. E. wrote the paper.

Conflicts of interest

There are no conflicts to declare.

Acknowledgements

Dr Elbuken acknowledges support from The Science Academy, Turkey, through the Young Scientist Award Program. Ziya Isiksacan is supported by ASELSAN Graduate Scholarship for Turkish Academicians. The authors acknowledge support from The Scientific and Technologic Research Council of Turkey (TUBITAK project no. 213S127). The authors thank Dr Amir H. Raffee, Ali Kalantarifard, Hazal Isiksacan, Mete Duman, Recep E. Ahan, Dr Bulend Ortac, Dr Rohat Melik, and Dr Gokhan Demirel for discussions and help.

References

- 1 World Health Organization, The top 10 causes of death, <https://www.who.int/news-room/fact-sheets/detail/the-top-10-causes-of-death>, (accessed 24 March 2020).
- 2 A. L. Copley and G. V. F. Seaman, *Clin. Hemorheol. Microcirc.*, 2016, **1**, 117–119.
- 3 Y. J. Kang and S. J. Lee, *Analyst*, 2018, **143**, 2723–2749.
- 4 H. J. Meiselman and O. K. Baskurt, *Semin. Thromb. Hemostasis*, 2003, **29**, 435–450.
- 5 O. K. Baskurt and H. J. Meiselman, *Clin. Hemorheol. Microcirc.*, 2013, **53**, 23–37.
- 6 Z. Xu, Y. Zheng, X. Wang, N. Shehata, C. Wang and Y. Sun, *Microsyst. Nanoeng.*, 2018, **4**, 17103.
- 7 Z. Xu, W. Dou, C. Wang and Y. Sun, *Microsyst. Nanoeng.*, 2019, **5**, 51.
- 8 Z. Isiksacan, M. T. Guler, A. Kalantarifard, M. Asghari and C. Elbuken, in *Biosensors and Nanotechnology*, John Wiley & Sons, Inc., Hoboken, NJ, USA, 2017, pp. 155–181.
- 9 Y. J. Kang, *Analyst*, 2016, **141**, 6583–6597.
- 10 Y. J. Kang, *Analyst*, 2019, **144**, 3556–3566.
- 11 H. Turlier, D. A. Fedosov, B. Audoly, T. Auth, N. S. Gov, C. Sykes, J. F. Joanny, G. Gompper and T. Betz, *Nat. Phys.*, 2016, **12**, 513–520.
- 12 Y. Qiu, D. R. Myers and W. A. Lam, *Nat. Rev. Mater.*, 2019, **4**, 294–311.
- 13 G. Tomaiuolo, *Biomicrofluidics*, 2014, **8**, 1–19.
- 14 J. Duez, M. Carucci, I. Garcia-Barbazan, M. Corral, O. Perez, J. L. Presa, B. Henry, C. Roussel, P. A. Ndour, N. B. Rosa, L. Sanz, F. J. Gamo and P. Buffet, *Nat. Protoc.*, 2018, **13**, 1362–1376.
- 15 G. M. Artmann, C. Kelemen, D. Porst, G. Büldt and S. Chien, *Biophys. J.*, 1998, **75**, 3179–3183.
- 16 P. H. Wu, D. R. B. Aroush, A. Asnacios, W. C. Chen, M. E. Dokukin, B. L. Doss, P. Durand-Smet, A. Ekpenyong, J. Guck, N. V. Guz, P. A. Janmey, J. S. H. Lee, N. M. Moore, A. Ott, Y. C. Poh, R. Ros, M. Sander, I. Sokolov, J. R. Staunton, N. Wang, G. Whyte and D. Wirtz, *Nat. Methods*, 2018, **15**, 491–498.
- 17 B. Fregin, F. Czerwinski, D. Biedenweg, S. Girardo, S. Gross, K. Aurich and O. Otto, *Nat. Commun.*, 2019, **10**, 415.
- 18 M. Dao, C. T. Lim and S. Suresh, *J. Mech. Phys. Solids*, 2003, **51**, 2259–2280.
- 19 Q. Guo, S. J. Reiling, P. Rohrbach and H. Ma, *Lab Chip*, 2012, **12**, 1143–1150.
- 20 H. W. Hou, A. A. S. Bhagat, A. G. L. Chong, P. Mao, K. S. W. Tan, J. Han and C. T. Lim, *Lab Chip*, 2010, **10**, 2605.
- 21 Y. Zheng, E. Shojaei-Baghini, A. Azad, C. Wang and Y. Sun, Proc. 16th Int. Conf. Miniaturized Syst. Chem. Life Sci. MicroTAS, 2012, vol. **2012**, pp. 398–400.
- 22 Z. Isiksacan, M. Asghari and C. Elbuken, *Microfluid. Nanofluid.*, 2017, **21**, 44.
- 23 A. Zhbanov and S. Yang, *PLoS One*, 2015, **10**, 1–25.
- 24 J. G. G. Dobbe, G. J. Streekstra, J. Strackee, M. C. M. Rutten, J. M. A. Stijnen and C. A. Grimbergen, *IEEE Trans. Biomed. Eng.*, 2003, **50**, 97–106.
- 25 Z. Isiksacan, O. Erel and C. Elbuken, *Lab Chip*, 2016, **16**, 4682–4690.

- 26 E. Kaliviotis, J. M. Sherwood and S. Balabani, *Sci. Rep.*, 2017, **7**, 44563.
- 27 G. Gompfer, F. Nicoud, D. A. Fedosov, S. Mendez, J.-M. Fromental, L. Lanotte, V. Claveria, J. Mauer and M. Abkarian, *Proc. Natl. Acad. Sci. U. S. A.*, 2016, **113**, 13289–13294.
- 28 M. E. Safar, *Nat. Rev. Cardiol.*, 2018, **15**, 97–105.
- 29 S. Varchanis, Y. Dimakopoulos, C. Wagner and J. Tsamopoulos, *Soft Matter*, 2018, **14**, 4238–4251.
- 30 M. Brust, C. Schaefer, R. Doerr, L. Pan, M. Garcia, P. E. Arratia and C. Wagner, *Phys. Rev. Lett.*, 2013, **110**, 078305.
- 31 A. Daly, J. S. Raval, J. H. Waters, M. H. Yazer and M. V. Kameneva, *Clin. Hemorheol. Microcirc.*, 2014, **56**, 337–345.
- 32 H. Huang, M. L. Yarmush and O. B. Usta, *Nat. Commun.*, 2018, **9**, 1–10.
- 33 A. D'Alessandro, G. Liunbruno, G. Grazzini and L. Zolla, *Blood Transfus.*, 2010, **8**, 82–88.
- 34 M. Musielak, *Clin. Hemorheol. Microcirc.*, 2009, **42**, 47–64.
- 35 E. Islamzada, K. Matthews, Q. Guo, A. T. Santoso, S. P. Duffy, M. D. Scott and H. Ma, *Lab Chip*, 2020, **20**, 226–235.
- 36 M. T. Guler, Z. Isiksacan, M. Serhatlioglu and C. Elbuken, *Sens. Actuators, B*, 2018, **273**, 350–357.
- 37 G. Oster and R. Zalusky, *Biophys. J.*, 1974, **14**, 124–129.
- 38 L.-G. Lindberg, *Opt. Eng.*, 1993, **32**, 253–257.
- 39 Z. Isiksacan, N. Hastar, O. Erel and C. Elbuken, *Sens. Actuators, A*, 2018, **281**, 24–30.
- 40 C. Miller, *Ind. Eng. Chem. Fundam.*, 1972, **11**, 524–528.
- 41 A. H. Raffiee, S. Dabiri and A. M. Ardekani, *Biomicrofluidics*, 2017, **11**, 064113.
- 42 A. H. Raffiee, S. Dabiri and A. M. Ardekani, *Microfluid. Nanofluid.*, 2019, **23**, 22.
- 43 M. Serhatlioglu, Z. Isiksacan, M. Özkan, D. Tuncel and C. Elbuken, *Anal. Chem.*, 2020, **92**, 6932–6940.
- 44 T. Go, H. Byeon and S. J. Lee, *Sci. Rep.*, 2017, **7**, 1–10.
- 45 A. H. Raffiee, S. Dabiri and A. M. Ardekani, *Phys. Rev. E*, 2017, **96**, 032603.
- 46 P. Yue, J. J. Feng, C. Liu and J. Shen, *J. Fluid Mech.*, 2005, **540**, 427–437.
- 47 P. Kelly, *Solid mechanics part I: An introduction to solid mechanics*, The University of Auckland, 2013.
- 48 B. Neu, R. Wenby and H. J. Meiselman, *Biophys. J.*, 2008, **95**, 3059–3065.
- 49 J. K. Armstrong, R. B. Wenby, H. J. Meiselman and T. C. Fisher, *Biophys. J.*, 2004, **87**, 4259–4270.
- 50 V. Tirtaatmadja, D. E. Dunstan and D. V. Boger, *J. Non-Newtonian Fluid Mech.*, 2001, **97**, 295–301.